Modeling and Development of a Biosensor Based on Optical Relaxation Measurements of Hybrid Nanoparticles

Stefan Schrittwieser,[†,*] Frank Ludwig,[‡] Jan Dieckhoff,[‡] Katerina Soulantica,[§] Guillaume Viau,[§] Lise-Marie Lacroix,[§] Sergio Mozo Lentijo,[§] Rym Boubekri,[§] Jérôme Maynadié,[§] Andreas Huetten,[⊥] Hubert Brueckl,[†] and Joerg Schotter[†]

[†]Molecular Diagnostics, AIT Austrian Institute of Technology, Vienna, Austria, [‡]Institute of Electrical Measurement and Fundamental Electrical Engineering, TU Braunschweig, Braunschweig, Germany, [§]Université de Toulouse, INSA, UPS, LPCNO, and CNRS, LPCNO, Toulouse, France, and [⊥]Department of Physics, Bielefeld University, Bielefeld, Germany

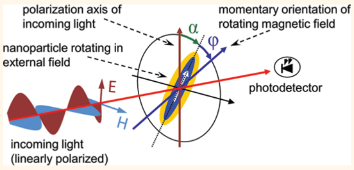

ABSTRACT We present a new approach for homogeneous real-time immunodiagnostics (denoted as "PlasMag") that can be directly carried out in sample solutions such as serum, thus promising to circumvent the need of sample preparation. It relies on highly sensitive plasmon-optical detection of the relaxation dynamics of magnetic nanoparticles immersed in the sample solution, which changes when target molecules bind to the surfaces of the nanoparticles due to the increase in their hydrodynamic radii. This method requires hybrid nanoparticles that combine both magnetic and optical anisotropic properties. Our model calculations show that core—shell nanorods with a cobalt core diameter of 6 nm, a cobalt core length of 80 nm, and a gold shell thickness of 5 nm are ideally suited as nanoprobes. On the one hand, the spectral position of the longitudinal plasmon resonance of such nanoprobes lies in the near-infrared, where the optical absorption in serum is minimal. On the other hand, the expected change in their relaxation properties on analyte binding is maximal for rotating magnetic fields as excitation in the lower kHz regime. In order to achieve high alignment ratios of the nanoprobes, the strength of the magnetic field should be around 5 mT. While realistic distributions of the nanoprobe properties result in a decrease of their mean optical extinction, the actual relaxation signal change on analyte binding is largely unaffected. These model calculations are supported by measurements on plain cobalt nanorod dispersions, which are the base component of the aspired core—shell nanoprobes currently under development.

KEYWORDS: magnetic nanoparticle · core—shell nanoparticle · nanorod · magnetic relaxation · biosensor

Magnetic nanoparticles (MNPs) offer a wide range of biomedical applications.[1,2] These particles are of interest for magnetic resonance imaging[3,4] as well as for drug delivery and targeting,[5] magnetic cell separation,[6] and hyperthermia cancer treatment.[7,8] Different approaches of biosensing in conjunction with MNP to detect proteins, DNA, cancer cell markers, and other biological and medical relevant targets can be found in literature.[9−13]

The term point-of-care (POC) diagnostics generally describes biomedical testing outside of clinical laboratories, which requires automated and robust analysis systems that display specific and sensitive results in a comprehensive format within a short time.[14] Today's gold standards in immunodiagnostics are heterogeneous assays like the enzyme-linked immunosorbent assay (ELISA). Though offering advantages such as low background, wide dynamic range, and high sensitivity for advanced ELISA test kits,[15] the required multiple incubation, filtration, and washing cycles render heterogeneous immunoassays slow and labor intensive,[16] thus preventing their widespread use for rapid POC testing.

Homogeneous immunoassays, on the other hand, offer the distinct advantage of utilizing simple "mix and measure" techniques. In a homogeneous assay, the binding of an analyte to its respective binder results in a direct change in signal.[17] For this reason, homogeneous assays do not require the numerous preliminary preparation steps usually executed for heterogeneous assays, which in principle allows to almost entirely skip sample preparation procedures.[18] In addition, homogeneous assays benefit from fast three-dimensional diffusion of both analyte and capture probes. This results in faster transition to equilibrium and more rapid testing than experienced for heterogeneous systems relying on two-dimensional diffusion of the analyte to the capture surface only. In addition, complicating issues like alignment control of the immobilized capture probes and steric hindrance of analyte binding to flat surfaces are not

* Address correspondence to stefan.schrittwieser.fl@ait.ac.at.

Received for review November 4, 2011 and accepted December 8, 2011.

10.1021/nn2042785

encountered for homogeneous immunoassays. Therefore, homogeneous assays are much more amenable to high-throughput screening and automated POC diagnosis.

We present a new nanoparticle-based approach (denoted as "PlasMag") for homogeneous real-time molecular detection.[19,20] The signal generated by functionalized nanoparticles (nanoprobes) is an increase of their average Brownian relaxation time upon binding analyte molecules, which is read out optically *via* anisotropic plasmon excitations within the nanoprobes. The measurement technique requires complex multicomponent nanoparticles that combine both magnetic and optical anisotropic properties. A suitable particle type would consist of an elongated core–shell structure with magnetic core and noble metal shell. Thereby, the magnetic core enables manipulation of the nanoprobe alignment by external magnetic fields, while the orientation-dependent excitation of the longitudinal plasmon mode of its anisotropic noble metal shell in polarized light allows optical detection of the actual nanoprobe alignment by extinction or scattering measurements (see results for gold (Au) nanorods described by Liz-Marzán[21]). Moreover, the noble metal shell serves as a protective coating against oxidation of the magnetic core and as a substrate for nanoparticle functionalization by specific antibodies against the target molecules. Since we are targeting *in vitro* immunodiagnostics, potential toxic effects of the nanoparticles on organisms can be reduced to the proper disposal of the sample material. A possible measurement mode employing a rotating magnetic field for alignment control of the nanoprobes is shown in Figure 1. Here, the signal would simply be the phase lag of the mean nanoparticle alignment with respect to the rotating magnetic field, which is a measure of the hydrodynamic drag of the nanoprobes in the carrier solution and increases upon the adhesion of analyte molecules.

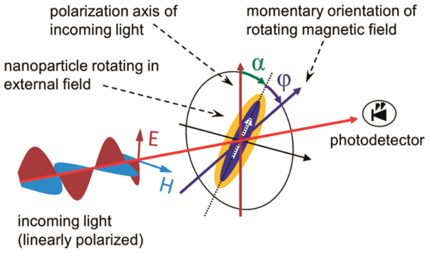

Figure 1. Schematic illustration of the "PlasMag" measurement principle. Nanoprobes follow the rotating external magnetic field at a certain phase lag φ, which depends on their hydrodynamic volume and increases on analyte binding. The angle φ follows from the measured transmission, which depends on the orientation of the nanoprobes' long axis with respect to the polarization direction of the incoming light (*i.e.*, the angle α).

The PlasMag concept is similar to magnetorelaxation (MRX)[11] or ac magnetometry[22,23]-based assays such as the magnetic relaxation immunoassay (MARIA)[24] or the immunomagnetic reduction assay (IMR),[25] which record the Brownian rotation of magnetic particle ensembles induced by time-varying external magnetic fields *via* measuring the total magnetic field they produce within a distant magnetic sensor. Due to the fast decay of this field with distance, relatively large concentrations of magnetic nanoparticles are required when using easily applicable magnetic sensor systems such as fluxgates (nanomolar range[11]). Only when employing complex SQUID-based sensors, nanoparticle sensitivities in the femtomolar range can be achieved[25] (SQUID: superconducting quantum-interference device). However, SQUID sensors are not well suited for POC applications due to the required liquid nitrogen cooling and the stringent requirements on sample handling and positioning.

Alternatively, magneto-optical relaxation of ferrofluids (MORFF) that makes use of the Cotton–Mouton effect of magnetic nanoparticles has been employed to achieve a relaxation sensor system with optical readout.[26,27] While signal generation and readout are similar to our proposed PlasMag concept, the small magnitude of the employed magneto-optical effect requires nanoparticle concentrations in the nanomolar range.[26] By introducing the complex multicomponent core–shell nanorods engineered for the PlasMag immunodiagnostic platform, we expect that the nanoprobe limit of detection will be enhanced to the subfemtomolar range due to the large scattering cross section inherent to the localized plasmon resonances excited within the noble metal shells (*e.g.*, Au) of these nanoprobes.[28]

Immunoassays detecting the spectral shift of the plasmon resonance in noble metal nanoparticles on the specific adhesion of analyte molecules have also been proposed[29] and developed.[30] However, due to the small magnitude of the spectral shift, the attainable detection limits of this method do not exceed the lower nanomolar range.[30]

In the present study, we discuss the optical, magnetic, and hydrodynamic properties of the required hybrid nanoparticles and, subsequently, the biosensing potential of our concept. While we currently seek to realize our aspired core–shell nanorods, optical transmission measurements on plain cobalt (Co) nanorods dissolved in organic solvents serve as a model system. Such Co nanoparticles can be fabricated with precise shape and size control from organometallic precursors.[31] Here, we employ single-crystalline Co nanorods with a fixed diameter of 6 nm and adjustable length.[32]

RESULTS AND DISCUSSION

Optical Nanorod Property Modeling. Analytical solutions (Mie theory) determining the scattering and extinction properties of nanoparticles are only available for a narrow range of particle geometries (i.e., ellipsoids), while for deviating geometries, numerical calculations have to be used. Our computations are based on the discrete dipole approximation (DDA).[33] Here, the particle is assumed to consist of an array of point dipoles, and the polarizability of each point depends on the dielectric function of the particle material. The interaction of incoming light with this array is then calculated in dependence of the dielectric function of the surrounding medium. According to literature, the DDA method generally agrees well to exact solutions,[33−35] which was also confirmed by us (see Experimental Methods).

Ideally, the measurement wavelength should lie in the near-infrared region, where the optical absorptions of both deoxyhemoglobin and normal saline solutions are minimal.[36] Specifically, common lasers with a wavelength of 1060 nm match this purpose, as the absorption in water and buffer solutions reaches a minimum at this wavelength.[37] Therefore, the longitudinal plasmon peak position of the employed nanorods should coincide with this laser wavelength. According to the DDA calculations of the extinction cross section of Co core/Au shell nanorods displayed in Figure 2a, this requirement can be met by particles consisting of a Co core with 6 nm diameter and 80 nm length coated by a 5 nm thick layer of Au. Here, the 5 nm Au shell thickness presents a good choice for high plasmon peak sharpness and sufficient layer thickness for passivating the magnetic core while still retaining the sensitivity of the particle's Brownian motion to analyte binding. Figure 2b shows the dependence of the nanorod extinction coefficient for different angles α of the nanorod's long axis with respect to the polarization axis of the incoming light. The extinction difference between perpendicular and parallel nanorod alignment reaches more than a factor of 250 for those rod dimensions, which assures large signal amplitudes when the mean orientation of the nanorod varies.

The calculations shown above were carried out for particles with perfectly homogeneous properties. The next step is to allow realistic variations of particle properties. Figure 3a shows the effect of Gaussian variations of both the length of the Co cores and the thickness of the Au shells on the extinction spectra of core−shell nanorods in water for longitudinal plasmon excitation. The assumed medium value μ and standard deviation σ of the Au shell thickness and the Co core length are indicated in the graph. While the variation of the Co core length is supported by a Gaussian fit to the data of a typical Co nanorod batch, a rather broad distribution is assumed for the Au shell thickness variation (σ/μ = 0.18 as opposed to σ/μ = 0.07 for the Co core length). As the synthesis method produces Co nanorods with well-defined diameter,[32] the Co core diameter was set constant to 6 nm for these DDA calculations.

While a variation of the Co core length only results in a decrease of the extinction cross section peak amplitude by about 14%, the strong dependence of the extinction cross section on the Au shell thickness also leads to a spectral shift. As the plasmon peaks of nanorods with thicker shells are blue-shifted and contribute more to the absolute extinction, the medium peak position is also blue-shifted. In total, the longitudinal plasmon resonance extinction maximum of the nanorods under variation of both the Au thickness and the Co core length decreases by about 27% in amplitude, blue shifts by about 26 nm relative to nanorods with no property variation, and the half-width maximum increases from 190 to 280 nm. From an experimental point of view, the spectral shift of the longitudinal plasmon peak of a specific nanorod ensemble can be compensated by adjusting the laser wavelength accordingly or modifying the mean Co core length, while the decrease in amplitude is not critical as single nanorod rotation is still expected to be observable by employing sensitive photomultiplier tubes in scattering geometry.[28]

Magnetic Nanorod Property Modeling. The Co nanorods employed here grow as single hcp crystals with the *c*-axis oriented along the long cylinder axis, and they are ferromagnetic at room temperature with saturation magnetization close to the bulk value of Co.[32] As both crystal and shape anisotropy are parallel, the remnant magnetization is oriented along the long nanoparticle axis and is almost identical to the saturation magnetization.[38]

The degree of alignment of nanorods with a magnetic moment m in a solution at a given field strength B_{mag} can be modeled by the Langevin equation:

$$L(m, B_{\mathrm{mag}}) = \coth\left(\frac{mB_{\mathrm{mag}}}{k_{\mathrm{B}}T}\right) - \frac{k_{\mathrm{B}}T}{mB_{\mathrm{mag}}}$$

For nanorods with ideal optical properties (*i.e.*, 80 nm Co core length), a magnetizing field of 5 mT is required to achieve 75% alignment. Thus, magnetic field strengths of up to 10 mT should be applicable by the measurement setup in order to achieve a sufficiently high degree of nanoprobe alignment.

Hydrodynamic Nanorod Property Modeling. Generally, the magnetization of an ensemble of magnetic nanoparticles can relax either by internal remagnetization of the particles (Néel relaxation, characteristic time scale τ_{N}) or by physical rotation of the nanoparticles in the carrier fluid (Brownian relaxation, characteristic time scale τ_{B}). The effective relaxation time τ_{eff} for a particle experiencing both Néel and Brownian relaxation is given by[39]

$$\tau_{\mathrm{eff}} = \frac{\tau_{\mathrm{B}}\tau_{\mathrm{N}}}{\tau_{\mathrm{B}} + \tau_{\mathrm{N}}}$$

For the Co nanorods regarded here, the magnetic shape and crystal anisotropy constants are collinear and sufficiently large that Néel type relaxation is entirely

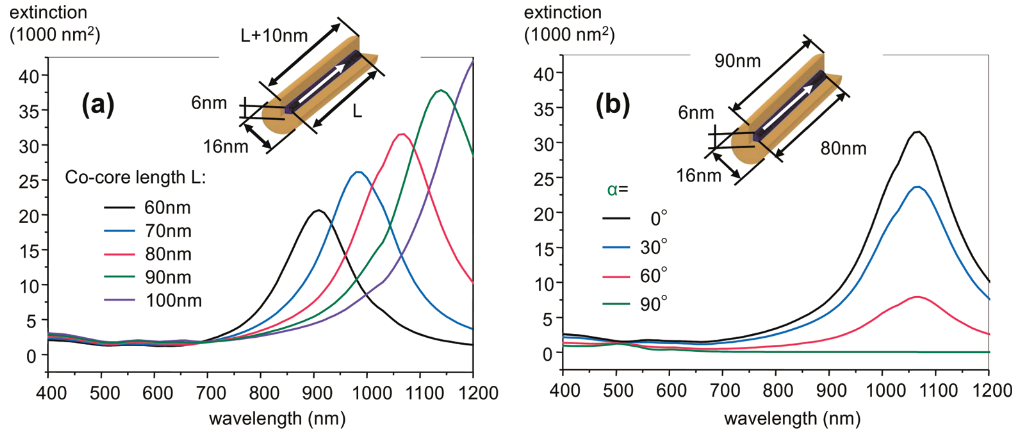

Figure 2. DDA calculations of the extinction cross sections of water-dispersed Co core/Au shell nanorods with a fixed Co core diameter of 6 nm. (a) Simulated extinctions (5 nm Au shell thickness) in dependence of the Co core length for incoming light with its polarization direction oriented parallel to the nanorods long axis. (b) Dependence of the extinction on the angle α between the long nanoparticle axis and the direction of polarization of the incoming light for nanorods with 80 nm Co core length and 5 nm Au shell thickness.

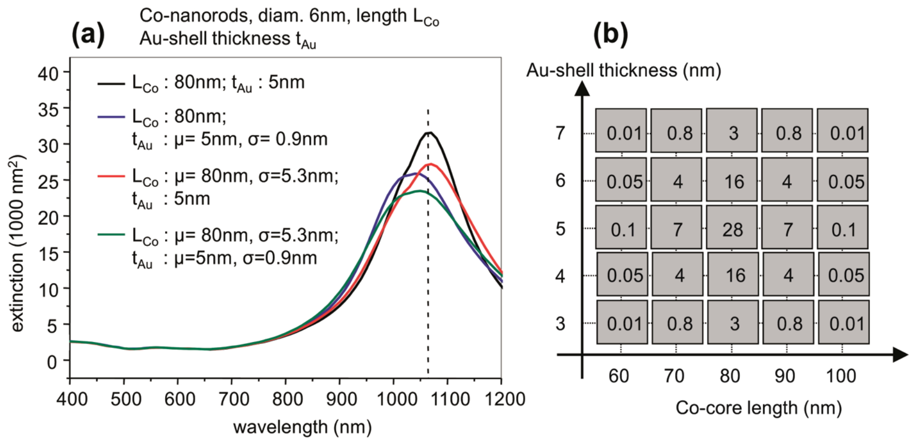

Au-shell thickness (nm)	60	70	80	90	100
7	0.01	0.8	3	0.8	0.01
6	0.05	4	16	4	0.05
5	0.1	7	28	7	0.1
4	0.05	4	16	4	0.05
3	0.01	0.8	3	0.8	0.01

Figure 3. (a) Changes of the longitudinal plasmon extinction peak for particles with Gaussian distribution (mean value μ, standard deviation σ) of the Au shell thickness (blue curve), the Co core length (red curve), and both the Au shell thickness and Co core length (green curve) relative to ideal nanorods with no geometry distributions (black curve). The curves are obtained by adding up the respective calculated extinction spectra of the discrete particle dimensions displayed in (b) according to their relative abundances (shown in each box).

quenched (the relaxation time is in the order of 10^{184} s). The remaining Brownian relaxation time can be defined by the rotational drag coefficient α according to[40]

$$\tau_B = \frac{\alpha}{2k_BT}$$

with temperature T and Boltzmann constant k_B.

For spheres with hydrodynamic volume V_{hydro}, the rotational drag coefficient in a fluid with dynamic viscosity η is given by

$$\alpha = 6\eta V_{hydro}$$

which yields

$$\tau_B = \frac{3\eta \cdot V_{hydro}}{k_BT}$$

For rigid cylinders with hydrodynamic length L_h and diameter d_h, the rotational drag coefficient has been derived as a model for macromolecules by Tirado *et al.*[41] according to

$$\alpha = \frac{\pi\eta L_h^3}{3}\left[\ln\frac{L_h}{d_h}+C\right]^{-1}$$

Here, C is an aspect-ratio-dependent end-cap correction term that can be approximated by

$$C = -0.662 + 0.891\frac{d_h}{L_h}$$

Modeling of the expected signal changes on analyte binding is carried out by calculating the Brownian relaxation time according to the rotational drag coefficient cited above. Thereby, molecules bound to the nanoparticles are treated as additional shells with a thickness representing the averaged volume equivalent size.

Modeling of Nanorod Rotational Behavior and Biosensing Potential. While magnetization processes within solids

SCHRITTWEISER *ET AL.* VOL. 6 ▪ NO. 1 ▪ 791–801 ▪ 2012 ACSNANO 794

are well described by the Gilbert equation,[42] thermal effects play a major role in ferrofluids. Considering thermal agitation in Gilbert's equation leads to the Fokker–Planck equation.[42] Another approach by Shliomis[43] demonstrates that the dynamics of the magnetization $\vec{M}$ of a small ferrofluid volume under the influence of a magnetic field $\vec{H}$ can also be described in a linear approximation (*i.e.*, small changes of the magnetization from equilibrium) by the following differential equation

$$\frac{d\vec{M}}{dt} = -\frac{1}{H^2\tau_{\mathrm{par}}}\vec{H}[(\vec{M} - \vec{M}_0)\vec{H}] - \frac{1}{H^2\tau_{\mathrm{perp}}}[\vec{H} \times (\vec{M} \times \vec{H})]$$

Here, the author assumes that the nanoparticles are rigid dipoles (*i.e.*, the magnetic moment m is fixed to the particle) and applied the effective field method. The equilibrium ferrofluid magnetization of particle concentration n is defined by

$$\vec{M}_0 = nmL(\xi)\frac{\vec{H}}{H} \text{ with } \xi = \frac{mH}{k_{\mathrm{B}}T}, \text{ and } L(\xi) = \coth(\xi) - \frac{1}{\xi}$$

For nanorods with a magnetic core length L_C and core diameter d_C, the magnetic moment is given by $m = M_S(\pi/4)d_C^2L_C$ with the saturation magnetization M_S.

The relaxation time constants parallel and perpendicular to the magnetic field take the following form:

$$\tau_{\mathrm{par}} = \tau_{\mathrm{B}}\frac{d\ln L(\xi)}{d\ln \xi} \text{ and } \tau_{\mathrm{perp}} = \tau_{\mathrm{B}}\frac{2L(\xi)}{\xi - L(\xi)}$$

For an external rotating magnetic field $\vec{H} = (H_0\cos(\omega_{\mathrm{H}}t), H_0\sin(\omega_{\mathrm{H}}t), 0)$ and assuming a constant phase lag φ, $\vec{M} = (M\cos(\omega_{\mathrm{H}}t - \varphi), M\sin(\omega_{\mathrm{H}}t - \varphi), 0)$, one obtains the following cubic equation for $x = \tan(\varphi)$:

$$x^3 - (\omega_{\mathrm{H}}\tau_{\mathrm{B}})x^2 + (1 + P)x - \omega_{\mathrm{H}}\tau_{\mathrm{B}} = 0 \text{ with}$$
$$P = \frac{1}{2}\xi L(\xi)$$

For small enough frequencies of the rotating magnetic field ($\omega_{\mathrm{H}}\tau_{\mathrm{B}} < 1$), the phase lag φ can be approximated by an arctan dependence:

$$\varphi = \arctan(\omega_{\mathrm{H}}\tau_{\mathrm{perp}})$$

Recently, Dieckhoff *et al.*[44] published an experimental verification of this phase lag dependence in rotating magnetic fields for spherical iron oxide nanoparticles sensed by fluxgate magnetometers.

Numerical solutions of the Fokker–Planck equation for a rotating magnetic field show that deviations from the solution given above get significant for high frequencies and large field amplitudes.[45] For the parameter range of practical relevance, the arctan dependence of the phase lag on frequency and time constant given above represents a good basis for the analytical modeling of the phase shift in dependence of analyte binding.

The evolution of the nanorod's phase lag φ with respect to a rotating magnetic field calculated by the arctan approximation is illustrated in Figure 4. For the saturation magnetization of Co, a value $M_S = 1.44 \times 10^6$ A/m was used.[46] Figure 4a shows the phase lag's dependence on the Co core length for increasing shell thicknesses, beginning with bare Co nanorods and ending up at fully antigen-loaded nanoprobes after subsequent shell addition (further parameters: field magnitude 1 mT, field frequency 1 kHz, water as medium with a viscosity of 1 mPa·s at 295 K). Nanoprobes of about 60–80 nm Co core length show the maximum phase change on binding of analyte molecules (up to 15° for a full 5 nm thick analyte coating). For longer nanorods, the relative phase difference decreases due to the reduced relative change in rotational drag coefficient on adding a constant layer thickness. The decreased relative phase difference for shorter nanorods can be understood in terms of increased angular disorder due to the stronger contribution of the thermal energy with respect to the magnetic energy. The frequency dependence of the phase lag for different added layer thicknesses for an 80 nm long Co core at 1 mT field amplitude is shown in Figure 4b. The largest phase changes are obtained at frequencies well below saturation, that is, in the lower kHz range.

When including multidispersity of the Co nanorods, the expected phase lag change on analyte binding decreases slightly, and the maximum phase lag change occurs at marginally higher frequencies. This is displayed in Figure 5, which shows the frequency dependence of the expected change in phase lag on binding of a 1 and 5 nm thick shell of antigens to nanorods with a Co core diameter of 6 nm and a 5 nm thick antibody functionalization. For monodisperse particles (solid curves), a homogeneous Co core length of 80 nm and a Au shell thickness of 5 nm are assumed, while the assumed Gaussian Co core length and Au shell variations for multidisperse particles (dashed lines) are identical to the ones described above (see Figure 3, other common parameters: field magnitude 1 mT, medium = water with viscosity of 1 mPa·s at 295 K). The resulting phase behavior for multidisperse particles is almost identical to monodisperse particles, and much stronger size variations than observed experimentally have to be included in order to obtain significant differences (see dotted lines). Therefore, the actual signal (*i.e.*, the phase lag change) is not expected to suffer from realistic particle variations.

Measurement Setup and Experimental Results. In brief, the rotating magnetic field is generated by two perpendicular Helmholtz coils (see Figure 6) which are sourced by the two channels of an audio power amplifier. The actual magnetic field is monitored by measuring each coil current *via* a shunt resistor, which allows adjusting the amplitudes and relative phases of the left and right output channel of the power amplifier

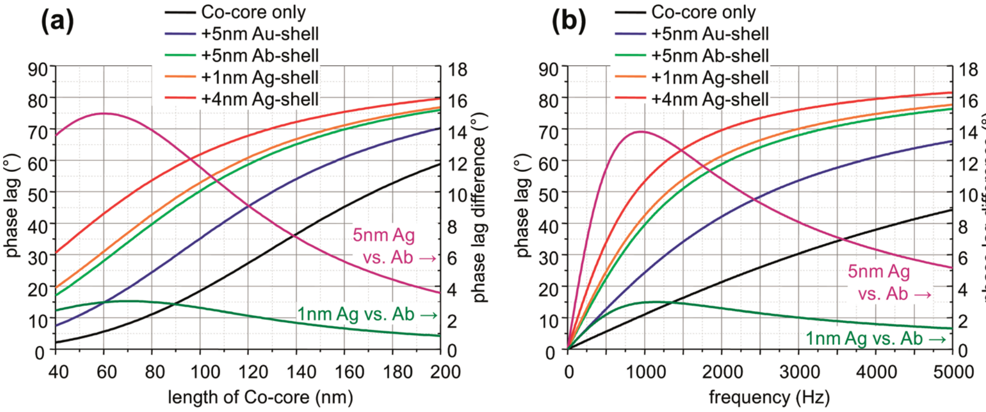

Figure 4. Calculated phase lag of nanorods following a rotating magnetic field. (a) Dependence on the Co core length for different states of the nanorods. These states are obtained from plain Co nanorods (black line) by subsequently adding a Au layer (blue line), an antibody (Ab) functionalization (green line), a partial antigen (Ag) shell (20% coverage with 5 nm sized Ag resulting in an effective layer thickness of 1 nm, orange line), and a full Ag coverage (5 nm Ag layer thickness in total, red line). The left axis represents the absolute phase lags, while the right axis indicates relative phase changes on Ag binding with respect to the Ab-functionalized state (20% Ag coverage, dark green; 100% Ag coverage, violet). (b) Dependence on the field frequency of a nanorod with 80 nm Co core length. The different nanorod states and axes are identical to part (a).

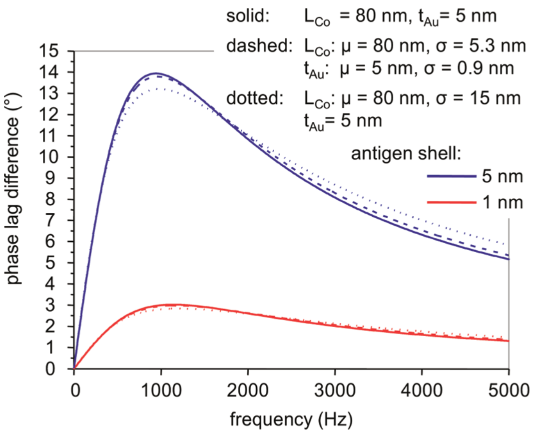

Figure 5. Effect of including multidispersity of the Co core/Au shell nanorods on the calculated phase lag difference to antibody-coated nanorods for two distinct amounts of bound analyte antigen molecules.

until a circular rotating magnetic field of desired strength is obtained at each frequency.

The main optical setup consists of a fiber-coupled laser diode and an output fiber that couples the transmitted light into a photodetector. The signal of the shunt resistor of the coil with its axis aligned parallel to the polarization direction of the incoming laser light and the output of the photodetector are fed into the reference and signal channel of a lock-in amplifier. Due to the cylindrical symmetry of the nanorods, the lock-in is set to measure the signal at the second harmonic of the reference frequency. Measurements of the signal phase and amplitude are carried out as a function of frequency and magnitude of the rotating magnetic field.

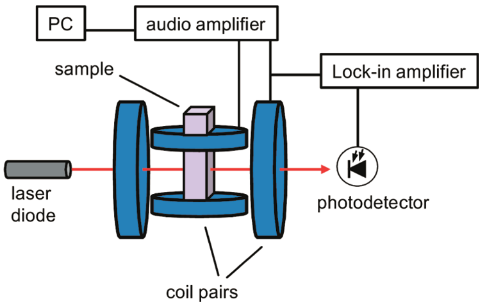

Figure 6. Schematic main PlasMag setup, including two orthogonally arranged pairs of Helmholtz coils, a fiber-coupled laser diode and a photodetector for transmission measurements. The photodetector output is measured by a lock-in amplifier. The sample cuvette is placed in the center of the coil setup.

For elongated particles, the optical polarizability depends on the orientation of their principal axis relative to the direction of the electric field. Thus, it is expected that optical observation of nanorod rotation in principle can also be carried out by plain Co nanorods. While analytic expressions can be derived for the anisotropic polarizability of ellipsoids,[47] the extinction cross sections of cylindrical particles can only be obtained by approximation. Here, we again employ the discrete dipole approximation[33] to calculate the spectral variation of the extinction cross sections C_{ext} and the transmissions $T = \exp(-nsC_{ext})$[47] of plain Co nanorods dissolved in toluene solution (refractive index 1.496) for parallel (T_{par}), perpendicular (T_{perp}), and random (T_{rand}) orientations of the long cylinder axis relative to the polarization of the incoming light. As the perpendicular orientation can be obtained *via* two degrees of freedom, the random transmission is given by $T_{rand} = (T_{par} + 2T_{perp})/3$.[48] Because the Co nanorods are stabilized by a surfactant layer of hexadecylamine (HDA), the calculations also include a 2 nm thick molecular shell with a refractive index of 1.5. These simulated transmission spectra (dashed lines in Figure 7)

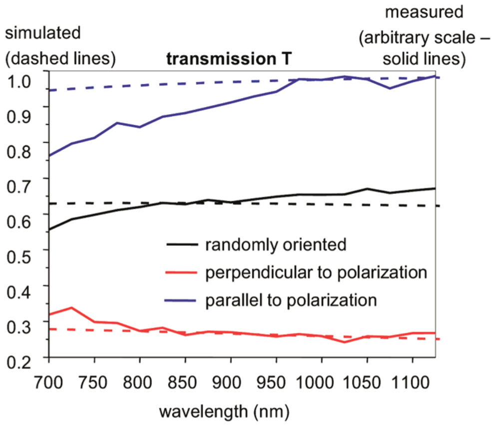

Figure 7. Comparison of simulated (dashed lines) and measured (solid lines) transmission spectra of Co nanorods for three different orientations of their long axis with respect to the direction of polarization of the incoming light. For the experimental curves, a static magnetic field of 15 mT strength is used for alignment control.

are compared to measured spectra (solid lines) of Co nanorods with a length of 90 nm at a particle density $n = 1.8 \times 10^{17}/\mathrm{m}^3$ (4 μg/mL). The optical path length s through the cuvette amounts to 1 cm. For the measured spectra, a homogeneous dc magnetic field with a magnitude of 15 mT is applied parallel and perpendicularly to the polarization direction of the incoming light, which is generated by a halogen lamp and analyzed by a spectrometer. The measured curves are also corrected for a linear time dependence caused by particle precipitation.

The simulated and measured spectral variations of the orientation-dependent transmissions of plain Co nanorods are in good qualitative agreement. In contrast to the localized plasmon resonance expected for Au-coated nanorods, the transmission of plain Co nanorods does not vary substantially within the relevant spectral range, so the light source does not need to be trimmed to a certain wavelength.

Typical results of the raw signals for transmission measurements carried out with the PlasMag setup for a rotating magnetic field are shown in Figure 8a (black line). The red line denotes the reference signal indicative of the rotating magnetic field component parallel to the polarization axis (voltage drop across the small Helmholtz coil's shunt resistor). Thus, the phase lag φ of the nanorod's long axis orientation relative to the rotating magnetic field refers to the time difference between the reference maximum and the minimum of the photodetector output with respect to the period of the rotating field. Phase lag measurements in rotating magnetic fields on nickel nanorods have also been presented recently by Guenther *et al.*[49]

Figure 8b shows the dependence of the nanorod phase lag on rotating field frequency for three different field magnitudes (straight lines, 53 nm medium nanorod length, 6 nm medium diameter, lauric acid (LA) as a ligand, tetrahydrofuran (THF) as solvent). As expected, the phase lag roughly follows the arctan (ω) dependence. Also, in accordance to the model, higher magnetic field magnitudes lead to lower phase lags due to the larger magnetic torque. When modeling the frequency dependence of the phase lag for single nanorods, phase lags much smaller than the measured ones are obtained (dotted lines in Figure 8b, right *y*-axis; viscosity of THF $\eta = 0.48$ mPas·s, 2 nm thick LA ligand shell, Co nanorod saturation magnetization M_S = 1440 kA/m). The reason is given by the formation of agglomerates. According to single particle tracking microscope measurements,[50] the mean hydrodynamic diameter of the particle agglomerates for this solution is d_h = 310 nm assuming spherical shape. This value was also confirmed by fluxgate MRX measurements. Therefore, in order to model the expected phase lag, a solution of spherical agglomerates with d_h = 310 nm is assumed. Hexagonally closely packed Co nanorods with a core diameter of 6 nm and a separation of 10 nm (*i.e.*, rod diameter + 2 × ligand shell thickness) correspond to a magnetic filling factor of about 1/3 of the hydrodynamic volume. Thus, for the model, we assume a spherical magnetic core volume with 213 nm diameter. With these values for d_h and d_c, the mean magnetization of the magnetic core is reduced until the calculated phase lag behavior approximately agrees to the measurements, which is achieved at 1/1000 of the saturation magnetization of Co (dashed lines in Figure 8b). Keeping in mind that single hexagonal rod arrays ("domains") can assemble into mostly compensated magnetic states (*i.e.*, neighboring rods with alternating magnetization directions[51]) and that several of these domains with different orientations can form a single agglomerate, such a strong magnetization decrease of an agglomerate relative to a single particle is a reasonable assumption. Additional characterization of the structural and magnetic properties of nanorod agglomerates is currently in progress.

Magnetic dipole–dipole interactions are the main reason for the agglomeration of the particles in suspension. These interactions fall off with increasing mean distance between two particles and at some point decrease below the thermal energy, which can be regarded as a stability limit of the particle dispersion.[52] For our base Co nanorods with optimum dimensions (*i.e.*, 80 nm length, diameter 6 nm) aligned collinearly by a magnetic field, the magnetic dipole–dipole interaction is equal to the thermal energy at a concentration of about 5 mg/mL (simplified model calculating the interaction between two particles only and translating the obtained limiting distance to a mean particle concentration assuming a cubic unit volume per particle; Co nanorods magnetized to saturation; room temperature = 295 K). Thus, we could expect that despite the large magnetic moment of our nanorods, it should still be feasible to prepare stable dispersions at the relevant particle concentrations. The

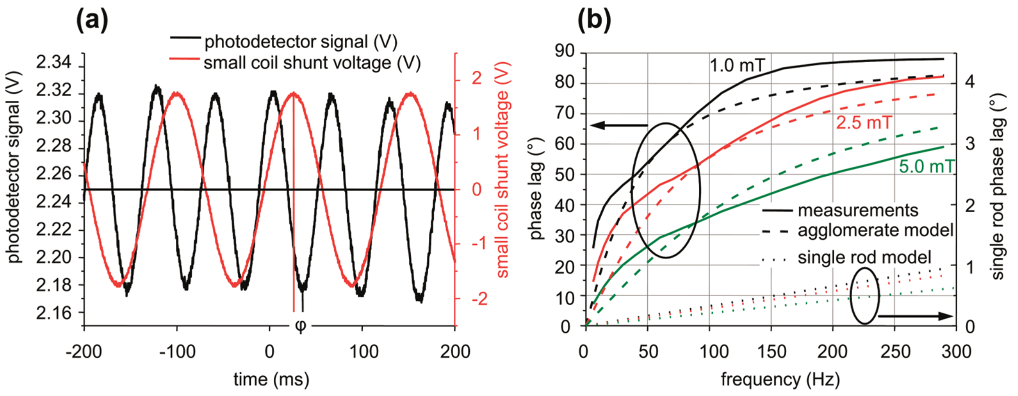

Figure 8. PlasMag transmission measurements on plain Co nanorod solutions in a rotating magnetic field. (a) Typical raw photodetector signal (black line) and reference representing one component of the rotating magnetic field (red line). (b) Dependence of the phase lag on rotating field frequency for three different field magnitudes (solid lines) and comparison to models (dashed/dotted lines; details given in the main text).

reason we still observe agglomeration in our measurements can be attributed to the synthesis procedure, during which the particles are periodically brought in close contact during separation steps applying a centrifuge. We are currently investigating alternative fabrication routes as well as improved stabilization protocols in order to avoid agglomeration and obtain colloidal suspensions consisting of single particles.

With our current setup in rotating magnetic field mode, we can resolve plain magnetic nanorod concentrations down to about 1 μg of Co per mL (defined by an upper accepted limit of the phase measurement's standard deviation <0.5°). For nanorods with a mean length of 80 and 6 nm diameter, this corresponds to a nominal particle concentration of ~100 pM. However, due to particle agglomeration and sedimentation, the nanorod concentration contributing to the measurement signal can be expected to be much lower. To estimate the actual sensitivity of our setup, we look at the measured amplitude for rotating nanorods in relation to the dc offset signal. For the same phase lag standard deviation limit applied above, extinction factors down to 1×10^{-4} can be resolved. Applying the transmission relation $T = I_{par}/I_{perp} = \exp(-ns\Delta C_{ext})$,[47] we obtain a measurable concentration limit for ideally dispersed Co nanorods of about $n = 20$ fM. Here, s is the optical path length through the sample cuvette (1 cm), I_{par} (I_{perp}) denote the measured intensity for nanorods aligned parallel (perpendicular) to the polarization of the incoming light, and ΔC_{ext} represents the respective calculated extinction cross section difference for Co nanorods with 80 nm length and 6 nm diameter in toluene solution. For Co nanorods with the same geometry covered by a 5 nm thick Au shell, the extinction cross section difference at the longitudinal plasmon resonance wavelength is calculated to be larger by a factor of 75, which accords to an expected measurable core–shell nanorod concentration limit of ~0.3 fM. For analyte binding to a nanoprobe surface coverage of 20%, we have calculated an expected phase lag change of ~3°, which is well above the employed standard deviation limit of 0.5°. For analytes with 5 nm size, this surface coverage corresponds to about 70 molecules bound per nanoprobe. Since the ratio of free to bound analyte molecules depends on a number of factors (*e.g.*, binding affinity), we conclude that, with our current setup, the maximum analyte detection limit is of the order of 20 fM. This value can be improved further by switching to scattering geometry and applying more sensitive photomultiplier tubes.

CONCLUSIONS

Our optical, magnetic, and hydrodynamic modeling of nanoprobes for the "PlasMag" biosensing principle reveals core–shell nanorods with a Co core length of 80 and 6 nm diameter coated by a 5 nm thick Au shell as most suitable. To address the most sensitive measurement regime, the PlasMag measurement setup should be capable to source rotating magnetic fields with magnitudes up to 10 mT and frequencies up to 3 kHz. Here, the expected maximum signal (*i.e.*, phase lag change of nanoprobes relative to magnetic field on analyte binding) for full analyte coverage amounts to ~14°, while typical signals for partial analyte loading are ~3–4°. Alternatively to the rotating magnetic field mode, it is also possible to apply linear ac magnetic fields as excitation. Compared to the rotating field mode, the optimal field frequency is reduced by a field-magnitude-dependent factor of up to two at 10 mT for the same particle geometries.

While the PlasMag principle has been demonstrated by measurements on plain Co nanorod suspensions in organic solvents, particle agglomeration still presents a major challenge. Alternative stabilization protocols following synthesis as well as application of different ligands to overcome this issue are currently in progress. Also, the targeted Au shells around the Co nanorods are expected to help in stabilizing the dispersions, enhance the optical signal by 2 orders of magnitude, and allow functionalization of antibodies to the nanorods by standard thiol chemistry. Furthermore, nanoporous alumina template-assisted fabrication of core−shell nanorods by subsequent atomic layer deposition of platinum[53] as plasmon resonance supporting shell material and iron oxide[54] as magnetic core material is presently under investigation.

EXPERIMENTAL METHODS

Co Nanorod Synthesis. The cobalt nanorods are synthesized according to Wetz *et al.*;[32] briefly the coordination compound [Co{N(SiMe$_3$)$_2$}$_2$], lauric acid (LA), and hexadecylamine (HDA) are mixed in an organic solvent in a Fischer−Porter pressure vessel in the interior of a glovebox. The vessel is closed and transferred to a vacuum line where after evacuation it is charged with H_2 under magnetic stirring. After charging, the vessel is closed and transferred to an oil bath already preheated to the reaction temperature for various time intervals. After the end of the reaction, the reactor is transferred in a glovebox and the solid is decanted. The supernatant is removed, and toluene is added in order to dissolve the superlattices of nanorods and the nanoparticles formed. By modification of the conditions employed (reaction time, temperature, H_2 pressure, Co/LA/HDA ratio, solvent), the mean length can be tuned from 25 to 180 nm. The nanocrystals are purified by centrifugation in order to separate the spherical nanoparticles from the nanorods. Following drying of the rods, they are redispersed in organic solvents such as toluene or THF (tetrahydrofuran) under further addition of ligands like HDA or LA.

Conditions for nanorods of 53 nm mean length: [Co{N(SiMe$_3$)$_2$}$_2$] (0.379 g, 1 mmol), HDA(0.241 g, 1 mmol), and LA (0.2 g, 1 mmol) were dissolved in 20 mL of dry toluene in a Fisher−Porter reactor. The reaction mixture was placed under 3 bar of H_2 and heated for 24 h at 120 °C in an oil bath under magnetic stirring.

Conditions for nanorods of 90 nm mean length: [Co{N(SiMe$_3$)$_2$}$_2$] (0.758 g, 2 mmol), HDA(0.482 g, 1 mmol), and LA (0.4 g, 1 mmol) were dissolved in 40 mL of dry anisole in a Fisher−Porter reactor. The reaction mixture was placed under 3 bar of H_2 and heated for 6 h at 150 °C in an oil bath under magnetic stirring.

Optical Extinction Calculations. The discrete dipole approximation[33] is employed in order to calculate the optical extinction spectra of different nanorod configurations. For each calculation, the lattice size is reduced until the obtained relative variation of the resulting extinction cross sections at each wavelength of the incoming light decrease below 1%. Absolute comparisons of the approximation to exact solutions according to the Mie theory have been carried out for spherical particles with different diameters. Due to the limited computational power, such systematic differences in extinction cross sections are allowed up to a limit of 3%. The calculations are carried out using the complex refractive index values for Au and Co by Palik,[55,56] and the nanorod is immersed in water as medium with a real refractive index of 1.333.

PlasMag Setup. The rotating magnetic field is generated by two perpendicular Helmholtz coils which are sourced by the two channels of an audio power amplifier (ATEC LAB power amplifier FP+14000BP). The input signal for the amplifier is generated by LabVIEW and sourced by a soundcard (E-MU Systems model 0404). Each coil is fed with a sinusoidal current, and the two currents possess a relative phase shift of 90°. For our perpendicular coil arrangement, this results in a rotating magnetic field under the condition that there is no phase shift between the current and the resulting magnetic field, which was verified experimentally. The magnetic field is controlled by measuring the current through each coil *via* the voltage drop across precision shunt resistors (Isabellenhuette RUG-Z, 0.5 Ω), which allows adjusting the amplitudes and relative phases of the left and right output channel of the power amplifier until a circular rotating magnetic field of desired strength is obtained at each frequency. Field magnitudes of 10 mT can be generated up to a maximum frequency of 430 Hz, 5 mT fields up to 1130 Hz, while frequencies higher than 2 kHz are possible for field magnitudes of 2.5 mT and below. In principle, higher magnitudes and frequencies can be obtained by setting up discrete resonant circuits.

The optical setup consists of a polarization maintaining fiber-coupled laser diode (OECA LQ7i-1060-25/BF2-FCSPC) with high polarization extinction ratio (30 dB) at 1060 nm, a collimator for sourcing the laser light into the sample cuvette and an output fiber that couples the transmitted light into a photodetector (New Focus Model 2011) *via* a focuser. The output fiber can also be positioned at a 90° angle with respect to the incoming light for measuring in scattering geometry. The optical components are positioned onto a benchtop vibration isolation platform and decoupled from the Helmholtz coils to avoid interference.

The signal of the shunt resistor of the coil with its axis aligned parallel to the polarization direction of the incoming laser light and the output of the photodetector are fed into the reference and signal channel of a lock-in amplifier (Signal Recovery DSP 7265). The second harmonic phase and amplitude are recorded in dependence of frequency and magnitude of the rotating magnetic field.

Spectrometer. Transmission spectra in static magnetic fields are measured by a Trax 550 spectrometer from JYHoriba.

Analysis of Hydrodynamic Particle Size. The NanoSight LM10 microscope with single particle tracking software was used with the ORCA Flash 2.8 video microscopy camera from Hamamatsu.

Acknowledgment. This work is supported by the European Commission FP7 NAMDIATREAM project (EU NMP4-LA-2010-246479) and has received funding by the European Commission FP6 SA-NANO (STRP 013698).

REFERENCES AND NOTES

1. Shubayev, V. I.; Pisanic, T. R.; Jin, S. Magnetic Nanoparticles for Theragnostics. *Adv. Drug Delivery Rev.* **2009**, *61*, 467–477.
2. Jain, K. K. Nanotechnology in Clinical Laboratory Diagnostics. *Clin. Chim. Acta* **2005**, *358*, 37–54.
3. Na, H. B.; Song, I. C.; Hyeon, T. Inorganic Nanoparticles for MRI Contrast Agents. *Adv. Mater.* **2009**, *21*, 2133–2148.
4. Xiao, L.; Li, J.; Brougham, D. F.; Fox, E. K.; Feliu, N.; Bushmelev, A.; Schmidt, A.; Mertens, N.; Kiessling, F.; Valldor, M.; *et al.* Water-Soluble Superparamagnetic Magnetite Nanoparticles with Biocompatible Coating for Enhanced Magnetic Resonance Imaging. *ACS Nano* **2011**, *5*, 6315–6324.
5. Liong, M.; Lu, J.; Kovochich, M.; Xia, T.; Ruehm, S. G.; Nel, A. E.; Tamanoi, F.; Zink, J. I. Multifunctional Inorganic Nanoparticles for Imaging, Targeting, and Drug Delivery. *ACS Nano* **2008**, *2*, 889–896.
6. Gijs, M. A. M. Magnetic Bead Handling On-Chip: New Opportunities for Analytical Applications. *Microfluid. Nanofluid.* **2004**, *1*, 22–40.
7. Barreto, J. A.; O'Malley, W.; Kubeil, M.; Graham, B.; Stephan, H.; Spiccia, L. Nanomaterials: Applications in Cancer Imaging and Therapy. *Adv. Mater.* **2011**, *23*, H18–H40.
8. Pankhurst, Q. A.; Thanh, N. K. T.; Jones, S. K.; Dobson, J. Progress in Applications of Magnetic Nanoparticles in Biomedicine. *J. Phys. D: Appl. Phys.* **2009**, *42*, 224001.
9. Haun, J. B.; Yoon, T.-J.; Lee, H.; Weissleder, R. Magnetic Nanoparticle Biosensors. *Wiley Interdiscip. Rev. Nanomed. Nanobiotechnol.* **2010**, *2*, 291–304.
10. Weddemann, A.; Albon, C.; Auge, A.; Wittbracht, F.; Hedwig, P.; Akemeier, D.; Rott, K.; Meissner, D.; Jutzi, P.; Huetten, A.

How To Design Magneto-Based Total Analysis Systems for Biomedical Applications. *Biosens. Bioelectron.* **2010**, *26*, 1152–1163.

11. Heim, E.; Ludwig, F.; Schilling, M. Binding Assays with Streptavidin-Functionalized Superparamagnetic Nanoparticles and Biotinylated Analytes Using Fluxgate Magnetorelaxometry. *J. Magn. Magn. Mater.* **2009**, *321*, 1628–1631.
12. Gao, J.; Gu, H.; Xu, B. Multifunctional Magnetic Nanoparticles: Design, Synthesis, and Biomedical Applications. *Acc. Chem. Res.* **2009**, *42*, 1097–1107.
13. Wang, S. X.; Li, G. Advances in Giant Magnetoresistance Biosensors with Magnetic Nanoparticle Tags: Review and Outlook. *IEEE Trans. Magn.* **2008**, *44*, 1687–1702.
14. Yager, P; Domingo, G. J.; Gerdes, J. Point-of-Care Diagnostics for Global Health. *Annu. Rev. Biomed. Eng.* **2008**, *10*, 107–144.
15. eBioscience Inc., product number BMS213HS.
16. Liu, X.; Dai, Q.; Austin, L.; Coutts, J.; Knowles, G.; Zou, J.; Chen, H.; Huo, Q. A One-Step Homogeneous Immunoassay for Cancer Biomarker Detection Using Gold Nanoparticle Probes Coupled with Dynamic Light Scattering. *J. Am. Chem. Soc.* **2008**, *130*, 2780–2782.
17. Diamandis, E. P.; Christopoulos, T. K. *Immunoassay*; Academic Press: San Diego, CA, 1996; pp 488−490.
18. Rowe, L.; Deo, S.; Shofner, J.; Ensor, M.; Daunert, S. Aequorin-Based Homogeneous Cortisol Immunoassay for Analysis of Saliva Samples. *Bioconjugate Chem.* **2007**, *18*, 1772–1777.
19. Schotter, J.; Bethge, O.; Maier, T.; Brueckl, H. Optische Messverfahren zur molekularen Detektion anhand von Relaxationsmessungen in optisch anisotropen Nanopartikeln. Austrian patent number 503.845, 2007, PCT application number WO/2008/124853.
20. Schrittwieser, S.; Schotter, J.; Maier, T.; Bruck, R.; Muellner, P.; Kataeva, N.; Soulantika, K.; Ludwig, F.; Huetten, A.; Brueckl, H. Homogeneous Biosensor Based on Optical Detection of the Rotational Dynamics of Anisotropic Nanoparticles. *Procedia Eng.* **2010**, *5*, 1107–1110.
21. Liz-Marzan, L. M. Tailoring Surface Plasmons through the Morphology and Assembly of Metal Nanoparticles. *Langmuir* **2006**, *22*, 32–41.
22. Enpuku, K.; Tamai, Y.; Mitake, T.; Yoshida, T.; Matsuo, M. AC Susceptibility Measurement of Magnetic Markers in Suspension for Liquid Phase Immunoassay. *J. Appl. Phys.* **2010**, *108*, 034701.
23. Oeisjoeen, F.; Schneiderman, J.; Astalan, A. P.; Kalabukhov, A.; Johansson, C.; Winkler, D. A New Approach for Bioassays Based on Frequency- and Time-Domain Measurements of Magnetic Nanoparticles. *Biosens. Bioelectron.* **2010**, *25*, 1008–1013.
24. Lange, J.; Koetitz, R.; Haller, A.; Trahms, L.; Semmler, W.; Weitschies, W. Magnetorelaxometry - A New Binding Specific Detection Method Based on Magnetic Nanoparticles. *J. Magn. Magn. Mater.* **2002**, *252*, 381–383.
25. Chieh, J. J.; Yang, S. Y.; Horng, H. E.; Yu, C. Y.; Lee, C. L.; Wu, H. L.; Hong, C. Y.; Yang, H. C. Immunomagnetic Reduction Assay Using High-Tc Superconducting-Quantum-Interference-Device-Based Magnetosusceptometry. *J. Appl. Phys.* **2010**, *107*, 074903.
26. Aurich, K.; Nagel, S.; Gloeckl, G.; Weitschies, W. Determination of the Magneto-Optical Relaxation of Magnetic Nanoparticles as a Homogeneous Immunoassay. *Anal. Chem.* **2007**, *79*, 580–586.
27. Buettner, M.; Weber, P.; Schmidl, F.; Seidel, P.; Roeder, M.; Schnabelrauch, M.; Wagner, K.; Goernert, P.; Gloeckl, G.; Weitschies, W. Investigation of Magnetic Active Core Sizes and Hydrodynamic Diameters of a Magnetically Fractionated Ferrofluid. *J. Nanopart. Res.* **2011**, *13*, 165–173.
28. Yguerabide, J.; Yguerabide, E. E. Light-Scattering Submicroscopic Particles as Highly Fluorescent Analogs and Their Use as Tracer Labels in Clinical and Biological Applications. *Anal. Biochem.* **1998**, *262*, 137–156.
29. Schotter, J.; Bethge, O.; Maier, T.; Brueckl, H. Recognition of Biomolecular Interactions by Plasmon Resonance Shifts in Single- and Multicomponent Magnetic Nanoparticles. *Appl. Phys. Lett.* **2008**, *93*, 144105.
30. Anfossi, L.; Baggiani, C.; Giovannoli, C.; Giraudi, G. Homogeneous Immunoassay Based on Gold Nanoparticles and Visible Absorption Detection. *Anal. Bioanal. Chem.* **2009**, *394*, 507–512.
31. Puntes, V. F.; Krishnan, K. M.; Alivisatos, A. P. Colloidal Nanocrystal Shape and Size Control: The Case of Cobalt. *Science* **2001**, *291*, 2115–2117.
32. Wetz, F.; Soulantica, K.; Respaud, M.; Falqui, A.; Chaudret, B. Synthesis and Magnetic Properties of Co Nanorod Superlattices. *Mater. Sci. Eng., C* **2007**, *27*, 1162–1166.
33. Draine, B. T.; Flatau, P. J. User Guide for the Discrete Dipole Approximation Code DDSCAT 6.1. arXiv.org e-Print archive; http://arxiv.org/abs/astro-ph/0409262v2, arXiv:0409262v2, 2004.
34. Draine, B. T.; Flatau, P. J. Discrete-Dipole Approximation for Scattering Calculations. *J. Opt. Soc. Am. A* **1994**, *11*, 1491–1499.
35. Purcell, E. M.; Pennypacker, C. R. Scattering and Absorption of Light by Nonspherical Dielectric Grains. *Astrophys. J.* **1973**, *186*, 705–714.
36. Kuenstner, J. T.; Norris, K. H. Spectrophotometry of Human Hemoglobin in the Near Infrared Region from 1000 to 2500 nm. *J. Near Infrared Spectrosc.* **1994**, *2*, 59–65.
37. Roggan, A.; Friebel, M.; Doerschel, K.; Hahn, A.; Mueller, G. Optical Properties of Circulating Human Blood in the Wavelength Range 400−2500 nm. *J. Biomed. Opt.* **1999**, *4*, 36–46.
38. Soulantica, K.; Wetz, F.; Maynadie, J.; Falqui, A.; Tan, R. P.; Blon, T.; Chaudret, B.; Respaud, M. Magnetism of Single-Crystalline Co Nanorods. *Appl. Phys. Lett.* **2009**, *95*, 152504.
39. Shliomis, M. I.; Raikher, Y. L. Experimental Investigations of Magnetic Fluids. *IEEE Trans. Magn.* **1980**, *16*, 237–250.
40. Debye, P. J. W. *Polar Molecules*; The Chemical Catalog Company Inc.: New York, 1929.
41. Tirado, M. M.; Garcia de la Torre, J. Rotational Dynamics of Rigid, Symmetric Top Macromolecules. Application to Circular Cylinders. *J. Chem. Phys.* **1980**, *73*, 1986–1993.
42. Coffey, W. T.; Cregg, P. J.; Kalmykov, Yu. P. On the Theory of Debye and Néel Relaxation of Single Domain Ferromagnetic Particles. *Adv. Chem. Phys.* **1993**, *83*, 263–464.
43. Shliomis, M. I. Ferrohydrodynamics: Retrospectives and Issues. In *Ferrofluids. Magnetically Controllable Fluids and Their Applications*; Odenbach, S., Ed.; Lecture notes in physics; Springer: Berlin, 2002; Vol. 594, pp 85−111.
44. Dieckhoff, J.; Schilling, M.; Ludwig, F. Fluxgate Based Detection of Magnetic Nanoparticle Dynamics in a Rotating Magnetic Field. *Appl. Phys. Lett.* **2011**, *99*, 112501.
45. Yoshida, T.; Enpuku, K.; Dieckhoff, J.; Schilling, M.; Ludwig, F. Magnetic Fluid Dynamics in a Rotating Magnetic Field. *J. Appl. Phys.*, submitted for publication.
46. Coey, J. M. D. *Magnetism and Magnetic Materials*; Cambridge University Press: Cambridge, United Kingdom, 2010.
47. Bohren, C. F.; Huffman, D. R. *Absorption and Scattering of Light by Small Particles*; Wiley-VCH: Weinheim, Germany, 2004.
48. Klein, T.; Laptev, A.; Guenther., A.; Bender, P.; Tschoepe, A.; Birringer, R. Magnetic-Field-Dependent Optical Transmission of Nickel Nanorod Colloidal Dispersions. *J. Appl. Phys.* **2009**, *106*, 114301.
49. Guenther, A.; Bender, P.; Tschoepe, A.; Birringer, R. Rotational Diffusion of Magnetic Nickel Nanorods in Colloidal Dispersions. *J. Phys.: Condens. Matter* **2011**, *23*, 325103.
50. NanoSight Ltd: Minton Park, London Road, Amesbury, Wiltshire, SP4 7RT, UK.
51. Dumestre, F.; Chaudret, B.; Amiens, C.; Respaud, M.; Fejes, P.; Renaud, P.; Zurcher, P. Unprecedent Crystalline Super-Lattices of Monodisperse Cobalt Nanorods. *Angew. Chem., Int. Ed.* **2003**, *42*, 5213–5216.
52. Bishop, K. J. M.; Wilmer, C. E.; Soh, S.; Grzybowski, B. A. Nanoscale Forces and Their Uses in Self-Assembly. *Small* **2009**, *5*, 1600–1630.

53. Henkel, C.; Aberman, S.; Bethge, O.; Bertagnolli, E. Atomic Layer-Deposited Platinum in High-*k*/Metal Gate Stacks. *Semicond. Sci. Technol.* **2009**, *24*, 125013.
54. Zierold, R.; Wu, Z.; Biskupek, J.; Kaiser, U.; Bachmann, J.; Krill, C. E.; Nielsch, K. Magnetic, Multilayered Nanotubes of Low Aspect Ratios for Liquid Suspensions. *Adv. Funct. Mater.* **2011**, *21*, 226–232.
55. Lynch, D. W.; Hunter, W. R. In *Handbook of Optical Constants of Solids*; Palik, E. D., Ed.; Academic Press: San Diego, CA, 1998; pp 286−295.
56. Ward, L. In *Handbook of Optical Constants of Solids II*; Palik, E. D., Ed.; Academic Press: San Diego, CA, 1998; pp 435−448.